








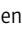

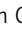


ARTICLE

Affinity maturation is required for pathogenic monovalent IgG4 autoantibody development in myasthenia gravis

Miriam L. Fichtner^{1,2*} , Casey Vieni^{3,4*} , Rachel L. Redler³ , Ljovica Kolich³ , Ruoyi Jiang² , Kazushiro Takata^{1,2} , Panos Stathopoulos^{1,2} , Pablo A. Suarez^{1,2} , Richard J. Nowak¹ , Steven J. Burden³ , Damian C. Ekiert^{3**} , and Kevin C. O'Connor^{1,2**} 

Pathogenic muscle-specific tyrosine kinase (MuSK)-specific IgG4 autoantibodies in autoimmune myasthenia gravis (MG) are functionally monovalent as a result of Fab-arm exchange. The development of these unique autoantibodies is not well understood. We examined MG patient-derived monoclonal autoantibodies (mAbs), their corresponding germline-encoded unmutated common ancestors (UCAs), and monovalent antigen-binding fragments (Fabs) to investigate how affinity maturation contributes to binding and immunopathology. Mature mAbs, UCA mAbs, and mature monovalent Fabs bound to MuSK and demonstrated pathogenic capacity. However, monovalent UCA Fabs bound to MuSK but did not have measurable pathogenic capacity. Affinity of the UCA Fabs for MuSK was 100-fold lower than the subnanomolar affinity of the mature Fabs. Crystal structures of two Fabs revealed how mutations acquired during affinity maturation may contribute to increased MuSK-binding affinity. These findings indicate that the autoantigen drives autoimmunity in MuSK MG through the accumulation of somatic mutations such that monovalent IgG4 Fab-arm-exchanged autoantibodies reach a high-affinity threshold required for pathogenic capacity.

Introduction

Myasthenia gravis (MG) is a chronic autoimmune disorder affecting neuromuscular transmission (Gilhus, 2016; Vincent, 2002). The disease is caused by pathogenic autoantibodies that target components of the neuromuscular junction. Given that the immunopathogenesis is directly governed by known autoantibody–autoantigen combinations, MG can serve as an archetype for B cell–mediated autoimmune disease. MG disease subsets are classified by autoantibody specificity; autoantibodies to the acetylcholine receptor (AChR; Vincent et al., 2000) are found in most patients, followed by autoantibodies to muscle-specific tyrosine kinase (MuSK) in other patients (Hoch et al., 2001). The clinical presentation among the subtypes is often similar, but the underlying immunopathology is decidedly divergent. The MuSK subtype highlights this distinction, as the autoantibodies in MuSK MG are primarily IgG4 (Niks et al., 2008), a subclass that does not share key properties found in the other subclasses. The most intriguing feature of human IgG4 antibodies is their unique ability to participate in antigen-binding fragment (Fab)–arm exchange, such that a

monospecific IgG4 antibody exchanges a heavy- and light-chain pair with another IgG4 antibody to become bispecific (van der Neut Kolfshoten et al., 2007). Consequently, IgG4 antibodies are asymmetric antibodies with two different antigen-combining sites and therefore possess monovalent specificities. Serum IgG4 autoantibodies that have undergone Fab-arm exchange (and are thus monovalent) contribute to the pathology of MuSK MG (Konecny et al., 2017). Although divalent MuSK monoclonal antibodies (mAbs) demonstrate pathogenic capacity using in vitro AChR clustering assays, they are not as effective as their monovalent counterparts (Huijbers et al., 2019). In addition, the divalent autoantibodies stimulate the phosphorylation of MuSK, whereas their monovalent counterparts, such as IgG4 autoantibodies in MuSK MG patient serum or monovalent Fabs, inhibit the phosphorylation of MuSK (Huijbers et al., 2013, 2019; Takata et al., 2019). The difference between the divalent and monovalent autoantibodies is likely due to the dual activity of the divalent antibodies, as they can dimerize MuSK, stimulate transphosphorylation (Herbst and Burden, 2000), and at the

¹Department of Neurology, Yale University School of Medicine, New Haven, CT; ²Department of Immunobiology, Yale University School of Medicine, New Haven, CT; ³Departments of Cell Biology and Microbiology, New York University School of Medicine, New York, NY; ⁴Medical Scientist Training Program, New York University School of Medicine, New York, NY.

*M.L. Fichtner and C. Vieni contributed equally to this paper; **D.C. Ekiert and K.C. O'Connor contributed equally to this paper; Correspondence to Kevin C. O'Connor: kevin.oconnor@yale.edu.

© 2020 Fichtner et al. This article is distributed under the terms of an Attribution–Noncommercial–Share Alike–No Mirror Sites license for the first six months after the publication date (see <http://www.rupress.org/terms/>). After six months it is available under a Creative Commons License (Attribution–Noncommercial–Share Alike 4.0 International license, as described at <https://creativecommons.org/licenses/by-nc-sa/4.0/>).

same time inhibit binding of low-density lipoprotein receptor-related protein 4 to MuSK.

During the course of a developing immune response to an exogenous antigen, B cells produce antibodies with increased affinity as they proceed through the process of affinity maturation (Neuberger, 2002; Rajewsky, 1996; Sarvas and Mäkelä, 1970). The successively greater antibody affinities accumulate as a direct result of clonal selection and the somatic hypermutation (SHM) process. B cell responses to self-antigen in most human autoimmune diseases appear to be products of this affinity maturation process. Autoantibodies with pathogenic capacity, isolated from patients with neuromyelitis optica, pemphigus vulgaris, or AChR MG, are characterized by the hallmarks of this process, including the accumulation of somatic mutations (Bennett et al., 2009; Di Zenzo et al., 2012; Graus et al., 1997). Recently, cloned autoantibodies that target MuSK were isolated from patients with MG (Huijbers et al., 2019; Stathopoulos et al., 2017; Takata et al., 2019). These autoantibodies show the hallmarks of affinity maturation, including accumulated somatic mutations. Given that IgG4 antibodies are often the product of a response to chronic exposure to exogenous antigens (Aalberse et al., 2009), such as allergens, it is not clear whether these autoantibodies are produced by B cells that were driven through the affinity maturation process by the autoantigen, MuSK. Moreover, given that IgG4 MuSK MG autoantibodies are functionally monovalent, as a consequence of Fab-arm exchange, the binding does not benefit from the accumulated strength of multiple affinities (avidity) that divalent antibodies use to their advantage. Thus, the affinity threshold for functional binding and pathogenic capacity may be higher than that of other autoantibodies and may consequently be highly dependent on affinity maturation.

We sought to further understand whether a self-antigen was driving the autoimmune response in MuSK MG. In particular, we determined how the SHM process contributes to MuSK autoantibody binding and pathogenic capacity in the context of both divalent and monovalent binding. We performed these experiments by examining a set of MuSK MG-derived human recombinant mAbs. These mAbs were reverted to their unmutated common ancestors (UCAs) by replacing all of the identifiable acquired somatic mutations with germline-encoded residues. They were expressed and evaluated as divalent mAbs or monovalent Fabs, the latter of which allowed us to directly test the properties of Fab-arm-exchanged products. We found that both mature and germline-encoded mAbs bound to MuSK and displayed pathogenic capacity. The mature monovalent Fabs also bound to MuSK and demonstrated pathogenic capacity. However, the germline-encoded Fabs bound to MuSK, but did not demonstrate measurable pathogenic capacity. The mature Fabs possessed very high affinity for MuSK, while the affinities of the germline-encoded Fabs were ~100-fold less than the mature Fabs. Crystal structures of two Fabs revealed that acquired somatic mutations in the mature Fabs increase the negative charge of the antigen-binding region, likely contributing to increased binding affinity to potential positively charged epitopes on MuSK. Taken together, these findings indicate that the autoantigen MuSK drives the autoimmune response in MuSK

MG. They furthermore demonstrate that IgG4 Fab-arm-exchanged MuSK autoantibodies require high-affinity binding to reach pathogenic capacity, establishing a particularly critical role for somatic mutations in these unique monovalent autoantibodies.

Results

UCAs of MuSK mAbs bind to the autoantigen MuSK

We previously isolated single B cells that expressed MuSK autoantibodies from two MuSK MG patients. From these single B cells, we produced human recombinant mAbs (MuSK1A, MuSK1B, and MuSK3-28) that bound to MuSK and demonstrated pathogenic capacity (Table S1; Stathopoulos et al., 2017; Takata et al., 2019). Here, we sought to investigate how affinity maturation contributed to MuSK binding. To this end, we reverted the mAbs to their putative germline configuration. Amino acid residue changes, arising from the SHM process, in the heavy and light variable region gene segments, including the templated regions of the CDR3s, were identified and mutated back to the UCA sequence configuration (Fig. 1 A). While somatic mutations in the untemplated regions of the CDR3 cannot be addressed, our experimental approach offered the best possible approximation of the germline configuration. The mutations were introduced in a stepwise manner; thus, we generated a series of mAbs in which only individual regions (complementarity-determining regions [CDRs] and framework regions [FRs]) or combinations of regions were changed to the germline configuration. This series of partially reverted mAbs (intermediate reversions) provided the opportunity for us to evaluate how different somatic mutations affected antigen binding. The mature mAbs, the intermediate reversions and the UCAs were tested for their ability to bind to MuSK using a live cell-based assay (CBA).

We compared the mature mAbs to their UCA counterparts (Fig. 1, B and C). These mAbs, as well as negative and positive control mAbs, were tested over a range of concentrations (10–0.02 $\mu\text{g/ml}$; Fig. 1 C). The mean fluorescence intensity (MFI) of MuSK antigen-transfected cells was subtracted from the MFI of nontransfected cells (ΔMFI). The UCAs of MuSK1A and MuSK1B antibodies and their mature counterparts bound to MuSK similarly; all four mAbs showing positive binding at concentrations as low as 0.02 $\mu\text{g/ml}$. The UCA of autoantibody MuSK3-28 showed diminished binding over this concentration range compared with its mature counterpart and was weakly positive from 10 to 0.2 $\mu\text{g/ml}$, while the mature mAb remained positive from 10 to 0.02 $\mu\text{g/ml}$.

Given that the UCA of mAb MuSK3-28 demonstrated diminished binding to MuSK, we next explored the binding of the intermediate reversion mAbs to evaluate how SHMs in the individual CDRs and FRs contributed to binding. We tested the intermediate reversions mAbs of MuSK1A, MuSK1B, and MuSK3-28, together with both negative and positive control mAbs over a range of mAb concentrations (10–0.02 $\mu\text{g/ml}$). Consistent with the results of the UCA binding, all intermediate constructs tested for MuSK1A bound MuSK similar to the mature mAb (Fig. S1 A). A number of the intermediates for MuSK1B showed a minor decrease in binding to MuSK. However, the

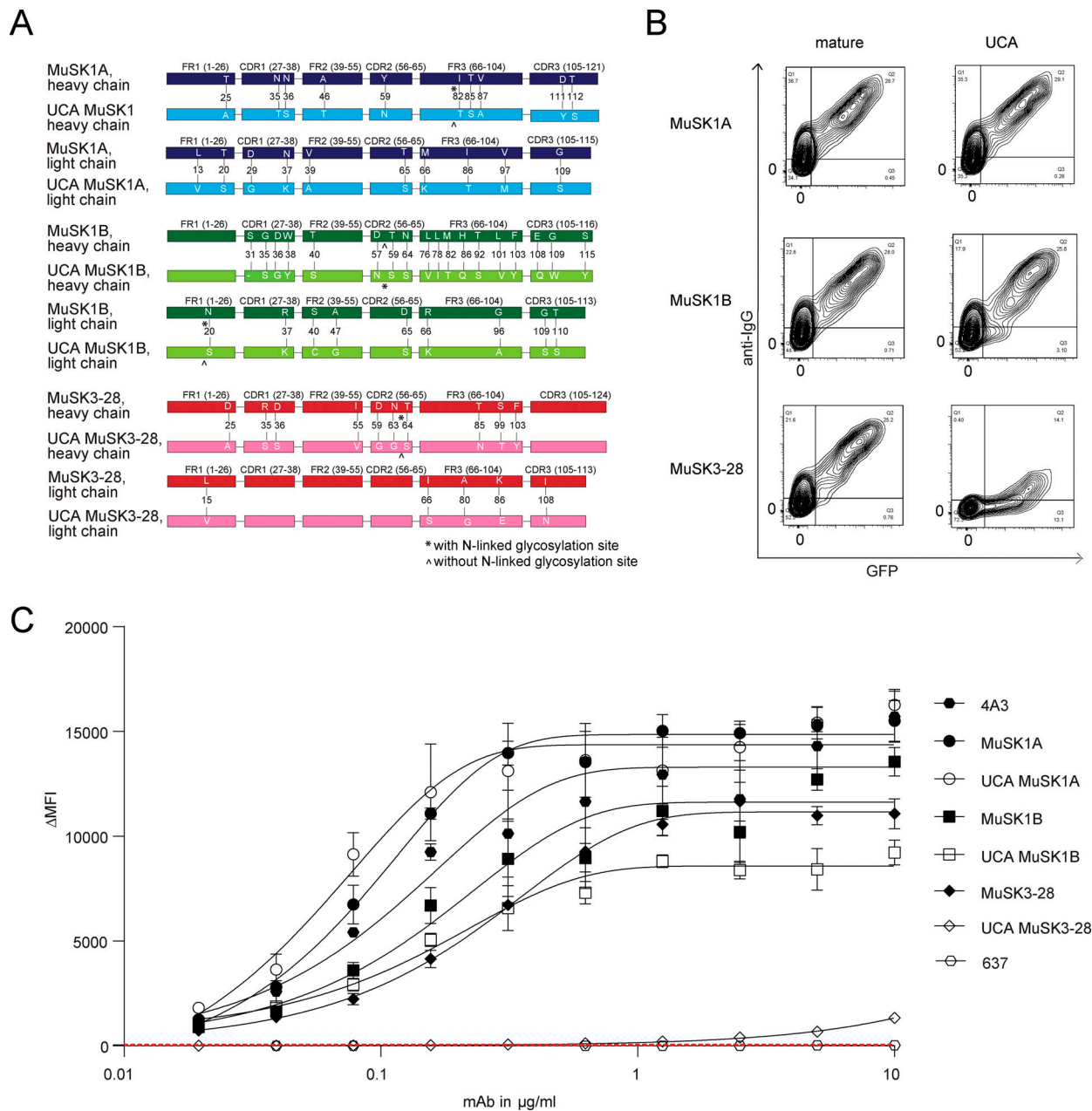


Figure 1. UCAs of MuSK mAbs bind to the MuSK autoantigen. MuSK-specific mAbs and their UCAs were tested for surface binding to MuSK on MuSK-GFP-transfected human embryonic kidney (HEK) cells. **(A)** Illustration of the differences in amino acid sequence between the mature mutated heavy and light chains compared with the UCA sequences. The different amino acids are shown in white letters. The number indicates the position of the amino acid within the variable region. The glycosylation sites are indicated with * if present and ^ if not present. **(B)** Representative CBA contour plots are shown for the three MuSK mAbs and their UCA. The x axis represents GFP fluorescence intensity and, consequently, the fraction of HEK cells transfected with MuSK. The y axis represents Alexa Fluor 647 fluorescence intensity, which corresponds to secondary anti-human IgG Fc antibody binding and, consequently, primary antibody binding to MuSK. Hence, transfected cells are located in the right quadrants and cells with MuSK antibody binding in the upper quadrants. The plots show testing with a mAb concentration of 1.25 $\mu\text{g/ml}$. **(C)** Binding to MuSK was tested over a series of 10 twofold dilutions of each mAb ranging from 10 to 0.02 $\mu\text{g/ml}$. Humanized MuSK mAb 4A3 was used as the positive control and AChR-specific mAb 637 as the negative control. The ΔMFI was calculated by subtracting the signal from nontransfected cells from the signal of transfected cells. Each data point represents the mean value from three independent experiments, and error bars represent SDs. Values greater than the mean + four SDs of the negative control mAb at 1.25 $\mu\text{g/ml}$ (indicated by the horizontal dotted line) were considered positive.

binding remained 1,639–2,183-fold above background at the concentration of 1.25 $\mu\text{g/ml}$, which we previously used to distinguish between binders and nonbinders (Fig. S1 B; Takata et al., 2019). Conversely, intermediate constructs for mAb

MuSK3-28 showed more pronounced changes in binding. The largest cause for diminished binding of MuSK3-28 could be attributed to a reversion of the H CDR1 and H CDR2 domain together with the H FR1, located close to the H CDR1 region of the

heavy chain. The Δ MFI of the mature mAb was 7,824, while the H CDR1 + CDR2 + FR1 reversion was 75 (104-fold decrease) at 1.25 μ g/ml (Fig. S1 C), which was similar to the UCA. Other reversions with either H CDR1 and H CDR2 alone or in combination with the H FR2 region did not show a substantial impact on binding.

We included a non-MuSK MG mAb to serve as a control. We reverted mAb 637 (a MG patient-derived recombinant monoclonal that recognizes AChR; Graus et al., 1997) back to the germline-encoded UCA sequence. A CBA specific for AChR was used to assess the binding to the AChR. The heavy chain CDR2 region germline reversion of mAb 637 showed diminished binding compared with the mature mAb 637 (Fig. S1 D). These results were reproducible over a broad range of concentrations. In summary, these findings demonstrate that UCA counterparts of the three MuSK mAbs all bind to MuSK.

The autoantibody light chains contribute to MuSK binding, and the UCAs bind to the same MuSK domain and are not polyspecific

We subsequently investigated whether the MuSK mAb light chains contribute to binding or if the binding is heavy chain dependent only. Therefore, all three mature MuSK mAb heavy chains were paired with nonendogenous light chains that were not originally paired with the heavy chain and tested for binding to MuSK by CBA. All of the mAbs with light chain swaps showed significantly diminished binding (P value range, 0.01–0.0001) compared with the endogenous pair (Fig. S1, E–G). The three mature mAbs (MuSK1A, MuSK1B, and MuSK3-28) recognized an epitope present in the Ig2-like domain of MuSK (Takata et al., 2019). We tested whether the UCA antibodies recognize the same epitope as their mature counterparts using several variants of the MuSK antigen. The extracellular region of MuSK is composed of three Ig-like domains and a frizzled-like domain (Fig. S2 A). Both the mature and UCA mAbs recognized the same domain (Ig2-like) on MuSK (Fig. S2, B and C). We next tested whether binding of the UCA mAbs was attributable to polyspecificity. Using a well-established approach, we tested reactivity against LPS, double-stranded DNA (dsDNA), and insulin by ELISA, as binding to all three of these antigens is a property of polyspecific antibodies (Wardemann et al., 2003). Binding to all three antigens was not observed for the three mature MuSK mAbs or their UCA counterparts (Fig. S3). In summary, the endogenous pairing of the heavy and light chain is important for binding, and both the mature and UCA mAbs recognize the same domain (Ig2-like) on MuSK and lack polyspecificity.

The UCA mAbs have lower affinity for MuSK than their mature counterparts

We next sought to measure the affinities of the antibodies to quantify and compare the strength of the antigen interaction between the mature MuSK mAbs and their UCAs. We produced monovalent Fabs to measure affinity, rather than avidity, and emulate the functional monovalency of Fab-arm-exchanged IgG4. All three mature Fabs displayed high affinity (equilibrium dissociation constant; K_D) for MuSK. Fab MuSK1A ($K_D = 0.41$ nM) and Fab MuSK1B ($K_D = 0.44$ nM) bound to MuSK with

Table 1. K_D values of mature and UCA Fabs MuSK1A, MuSK1B, and MuSK3-28

	K_D of mature Fab (nM)	K_D of unmutated ancestor Fab (nM)	Fold change
MuSK1A	0.41 \pm 0.0045	31 \pm 0.21	76
MuSK1B	0.44 \pm 0.0040	53 \pm 0.59	120
MuSK3-28	12 \pm 0.022	870 \pm 12	73

30 times higher affinity than Fab MuSK3-28 ($K_D = 12$ nM; Fig. S4, A, C, and E). The UCAs of all three mature Fabs had a lower affinity for MuSK than the mature Fabs (Table 1). The affinity of UCA Fab MuSK1A for MuSK dropped 76-fold ($K_D = 31$ nM); the affinity of UCA Fab MuSK1B dropped 120-fold ($K_D = 53$ nM); the affinity of UCA Fab MuSK3-28 decreased by 73-fold ($K_D = 870$ nM; Fig. S4, B, D, and F). The dissociation rates were faster for the UCA Fabs of MuSK1A and MuSK1B compared with their mature counterparts (Table 2). The comparison of the UCA and mature Fab of MuSK3-28 (Table 2) showed a slower association rate and similar dissociation rate. Overall, the increased affinity of the mature MuSK3-28 Fab was mainly the consequence of a faster association rate, while the increased affinity of MuSK1A and MuSK1B was largely due to reduced dissociation rates. In summary, the binding kinetics of the UCA and mature Fabs show altered association or dissociation rates that contribute to an \sim 100-fold change in affinity.

Crystal structures of MuSK1A and MuSK1B Fabs

To understand the structural basis for how affinity maturation contributes to MuSK binding, we obtained crystals of MuSK1A and MuSK1B to 1.8 Å and 1.75 Å, respectively (Fig. 2, A and B; and Table S2). The overall structures of both MuSK1A and MuSK1B were comparable to a number of Fabs with high CDR amino acid sequence similarity found in the Protein Data Bank (PDB; Fig. S5). Compared with these sequence-related Fabs, MuSK1A and MuSK1B differed most significantly in the heavy and light CDR3 loops, consistent with these loops being the sites of greatest diversification in most antibodies. For both MuSK1A and MuSK1B, the mutations away from the UCA sequence were distributed throughout the Fab variable domains, with \sim 40–50% of the mutations clustered in the CDR loops and the remainder scattered throughout the FRs (Fig. 2, C and D). In the crystal structure for MuSK1B, we observed blurred electron density in the vicinity of the heavy chain “elbow” region, which connects the variable (VH) and constant (CH1) domains of an antibody. Blurred electron density was observed for the linker between the VH and CH1 domains, as well as several nearby turns between strands of the VH domain regions. The lower quality of electron density in this local area likely indicated flexibility or multiple conformations within this region.

Immunoglobulins can contain glycans within the variable region (van de Bovenkamp et al., 2016). Consensus amino acid motifs (N-X-S/T) for N-linked glycosylation sites can either be present within the germline sequence or acquired during the SHM process. Enrichment of Fab glycans has been observed in

Table 2. k_{on} and k_{off} values of mature and UCA Fabs MuSK1A, MuSK1B, and MuSK3-28

	k_{on} ($M^{-1} s^{-1}$)	k_{off} (s^{-1})
MuSK1A	$3.2 \pm 0.03 \times 10^5$	$1.3 \pm 0.007 \times 10^{-4}$
UCA MuSK1A	$5.7 \pm 0.04 \times 10^5$	$1.8 \pm 0.003 \times 10^{-2}$
MuSK1B	$4.3 \pm 0.04 \times 10^5$	$1.9 \pm 0.008 \times 10^{-4}$
UCA MuSK1B	$4.0 \pm 0.04 \times 10^5$	$2.1 \pm 0.006 \times 10^{-2}$
MuSK3-28	$1.4 \pm 0.003 \times 10^5$	$1.6 \pm 0.001 \times 10^{-3}$
UCA MuSK3-28	$0.022 \pm 0.0003 \times 10^5$	$1.9 \pm 0.009 \times 10^{-3}$

k_{on} , association rate; k_{off} , dissociation rate.

autoimmunity (Koers et al., 2019; van de Bovenkamp et al., 2018). While conserved N-linked glycosylation sites are present in the antibody Fc regions, glycosylation of the variable domains is less common. Based upon their amino acid sequences, during affinity maturation, all three mature MuSK mAbs (Fig. 1 A) were predicted to acquire or retain glycosylation sites within the variable regions (Blom et al., 2004), either in the heavy (MuSK1A and 3-28) or light chain (MuSK1B). The UCA of MuSK1B had an additional N-linked glycosylation site within the heavy chain that was lost during affinity maturation (Fig. 1 A). Our electron density maps provided unambiguous experimental evidence that N81 of MuSK1A heavy chain and N20 of MuSK1B light chain were modified by N-linked glycosylation (Fig. 2, E and F). Carbohydrate residues could be modeled into additional electron density in MuSK1A at residue N81 of the heavy chain (Fig. 2 E), including the first two N-acetylglucosamine residues and a β -D-mannose. In our mature MuSK1B structure, we were able to model the first N-acetylglucosamine residues (Fig. 2 F).

We next sought to understand how affinity maturation could play a role in MuSK MG pathogenesis. Interestingly, the mature MuSK1A light chain and, to a lesser extent, mature MuSK1A heavy chain CDR loops were largely negatively charged (Fig. 2 G), while the germline sequence in the CDR regions may have more neutral or additional positive charge (Fig. 2 H). For example, G28D in L CDR1, Y101D in H CDR3, or K30N in L CDR1 might make this region more negatively charged, while K52M in L CDR2 might serve to neutralize positive charge present in the UCA sequence. Similarly, the mature MuSK1B CDR loops were largely negatively charged (Fig. 2 G), while sequence-related Fabs to the UCAs tend to be largely positively charged (Fig. 2 H); hence, the mutations from the UCA to the mature Fab might serve to increase the negative charge of the CDR regions. For example, the mutations S51D in L CDR2, and G32D and S57N, respectively, in H CDR1 and H CDR2, might all increase the negativity of the antigen-binding site. Notably, the MuSK Ig1-like domain is predominantly negative, while the MuSK Ig2-like domain is highly positively charged (Fig. 2 I; Stiegler et al., 2006). As the MuSK1A and MuSK1B epitopes have been mapped at the domain level to the MuSK Ig2-like domain (Takata et al., 2019), this might suggest that MuSK1A and MuSK1B likely bind to one or both of the basic patches on the Ig2-like domain of MuSK. In summary, these collective structural data indicate that

the MuSK1A and MuSK1B Fabs share common structural features with Fabs of similar composition and include occupied variable region glycosylation sites. These findings further suggest that acquired mutations may strengthen the binding affinity for the basic patches on the MuSK Ig2-like domain by altering the electrostatic interactions at the antigen-antibody interface.

The pathogenicity of the MuSK autoantibodies is dependent on both affinity and valency

We next sought to evaluate how the amino acid changes resulting from SHM contributed to pathogenicity. We previously demonstrated that all three mature mAbs are pathogenic when tested using an established in vitro AChR clustering assay (Takata et al., 2019). Accordingly, we investigated whether the UCA counterparts of the mature mAbs disrupt AChR clustering in C2C12 myotubes. In addition to the divalent mAbs, we tested whether the amino acid substitutions from SHM had an impact on pathogenicity by testing the mature and UCA monovalent Fabs, which emulated Fab-arm-exchange products.

C2C12 myotubes were incubated with agrin, the neuronal ligand that stimulates AChR clustering, together with MuSK mAbs, MuSK Fabs, and control antibodies. AChR clusters were visualized and the mean number of AChR clusters quantified. The number of AChR clusters that formed in response to agrin alone was assigned a value of 100%, and the number of AChR clusters that formed in the presence of the antibodies was expressed relative to this value. The UCA of MuSK1A reduced the number of AChR clusters by 67.1% ($P < 0.0001$) and the UCA of MuSK1B by 73.0% ($P < 0.0001$; Fig. 3, A and B). Although mature MuSK3-28 reduced the number of AChR clusters by 49.7% ($P < 0.001$), the UCA of MuSK3-28, unlike the other UCAs, failed to diminish the number of AChR clusters that formed in response to agrin (percentage of agrin effect, 98.3; Fig. 3 B). The Fabs from the mature MuSK1A (percentage of agrin effect, 1.4) and MuSK1B antibodies (percentage of agrin effect, 1.5) reduced AChR clustering to near-background values ($P < 0.0001$; Fig. 3 B). The UCA Fabs of MuSK1A and MuSK1B, however, had modest pathogenic capacity (AChR clustering was reduced by ~20% by each of them; Fig. 3 B). In contrast, the Fabs from mature and UCA MuSK3-28 failed to inhibit agrin-induced AChR clustering (Fig. 3 B). We next evaluated further whether the UCA and mature Fabs inhibit AChR clustering differently by comparing them directly to each other. The Fab of MuSK1A inhibited AChR clustering by 98.6%, while the UCA Fab of MuSK1A inhibited AChR clustering by 22.1% (Welch's t test, $P = 0.0071$). Similarly, the Fab of MuSK1B inhibited AChR clustering by 98.5%, while the UCA Fab of MuSK1B inhibited AChR clustering by 18.9% (Welch's t test, $P = 0.0136$). In summary, the UCA of MuSK1A and MuSK1B mAbs demonstrated pathogenic capacity, but the UCA of the lower-affinity mAb MuSK3-28 did not. However, in the monovalent configuration, which emulates Fab-arm exchange, only the mature, high-affinity MuSK1A and MuSK1B antibodies were able to significantly disrupt agrin-induced AChR clustering, thus demonstrating pathogenetic capacity.

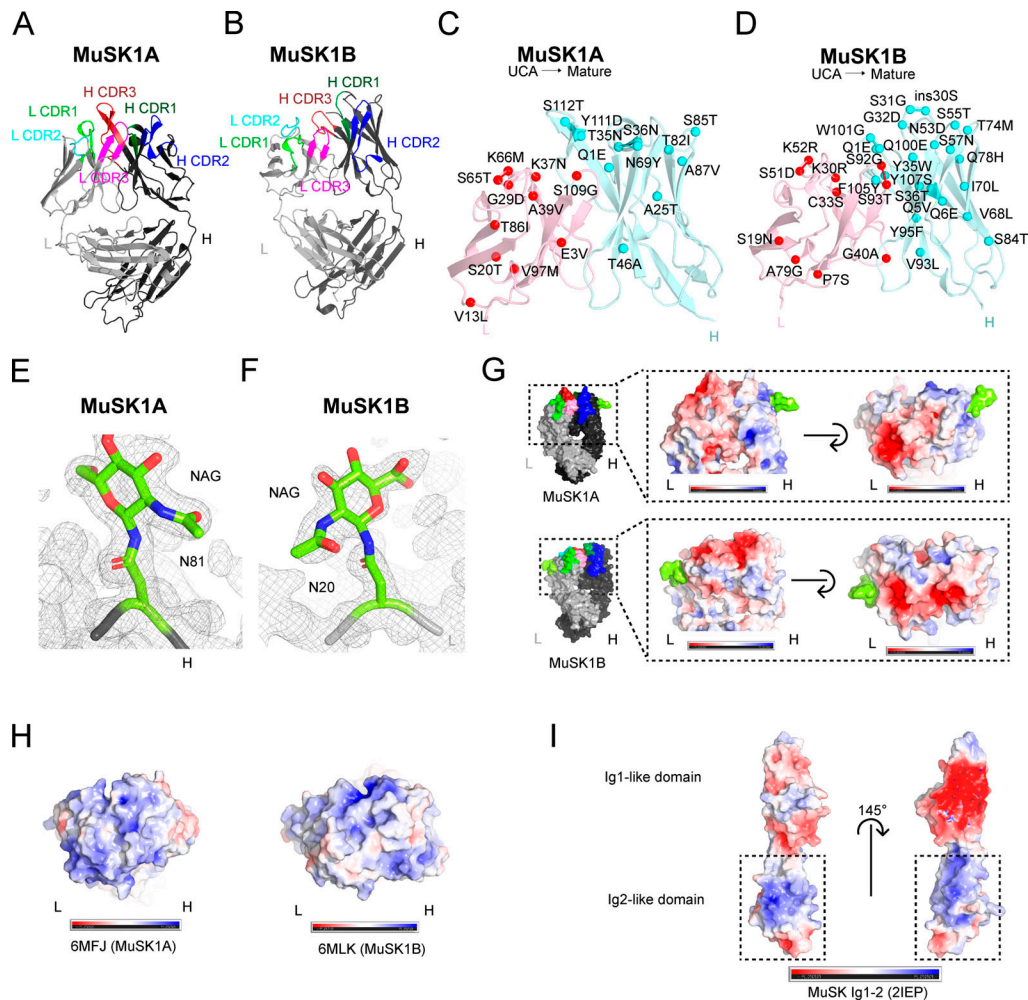


Figure 2. Crystal structure, mutation map, and glycosylation and electrostatic potential maps of MuSK1A, MuSK1B, and the MuSK Ig1-2-like domain. **(A)** Structure of MuSK1A heavy and light chains (PDB: 6WYR). **(B)** Structure of MuSK1B heavy and light chains (PDB: 6WYT). **(C)** UCA mutations mapped to the mature MuSK1A. UCA mutations are scattered throughout the mature MuSK1A CDR and FR regions. The MuSK1A light chain is colored light pink, and the MuSK1A heavy chain is colored pale cyan. UCA mutant C_α carbons are shown as darker red or cyan spheres for the light or heavy chain, respectively, with the mutation from the UCA to the mature mAb. **(D)** UCA mutations mapped to mature MuSK1B. UCA mutations are uniformly distributed throughout the mature MuSK1B CDR loops and FR regions. **(E)** N81 glycosylation site in the MuSK1A heavy chain at a threshold of 1.0 σ in the 2Fo-Fc map. The MuSK1A heavy chain backbone is shown as a black tube. **(F)** N20 glycosylation site in the MuSK1B light chain at a threshold of 1.0 σ in the 2Fo-Fc map. MuSK1B light-chain backbone is shown as a light gray tube. **(G)** Electrostatic potential map of MuSK1A and MuSK1B at the antigen-binding site with the modeled glycans shown in yellow green. In MuSK1A, the light chain is predominantly negatively charged, while in MuSK1B, both the heavy and light chains are predominantly negatively charged. **(H)** Electrostatic potential map of sequence-related Fabs for UCA MuSK1A (PDB code: 6MFJ) and UCA MuSK1B (PDB code: 6MLK) at the antigen-binding site. **(I)** Electrostatic potential map of the MuSK Ig1-like and Ig2-like domains. The MuSK Ig1-like domain is predominantly negative, while the MuSK Ig2-like domain has two positively charged patches.

Discussion

To further understand the mechanisms underlying autoimmune MG pathology, we recently identified and isolated a set of B cells from MuSK MG patients. Whole recombinant human mAbs from these cells were expressed, and then their specificity and pathogenic capacity was confirmed (Stathopoulos et al., 2017; Takata et al., 2019). In the current study, we used these mAbs to investigate the evolution of the autoantibody response in MuSK MG. We reverted the identifiable somatic mutations of the mAbs back to their putative germline configuration, thus generating UCAs. We also expressed whole IgG and their Fabs so that we could test the contribution of somatic mutations to both monovalent and divalent binding, thus emulating the products of Fab-

arm exchange from IgG4 antibodies. With this array of autoantibody constructs, we tested binding to the autoantigen, pathogenic capacity, and the affinity between the autoantibody and the cognate self-antigen. We found that the UCAs of MuSK autoantibodies can demonstrate strong binding to MuSK, suggesting that MuSK may drive SHM. The endogenous heavy and light chain combination was required for this binding. The binding was not a product of polyspecificity, and the UCAs recognized the same domain on MuSK as the mature mAbs. The UCAs of two mAbs displayed pathogenic capacity similar to what was observed with mature mAbs, but only when they were presented to the antigen as dimeric mAbs and not as monovalent Fabs. Affinity measurements demonstrated that the SHM

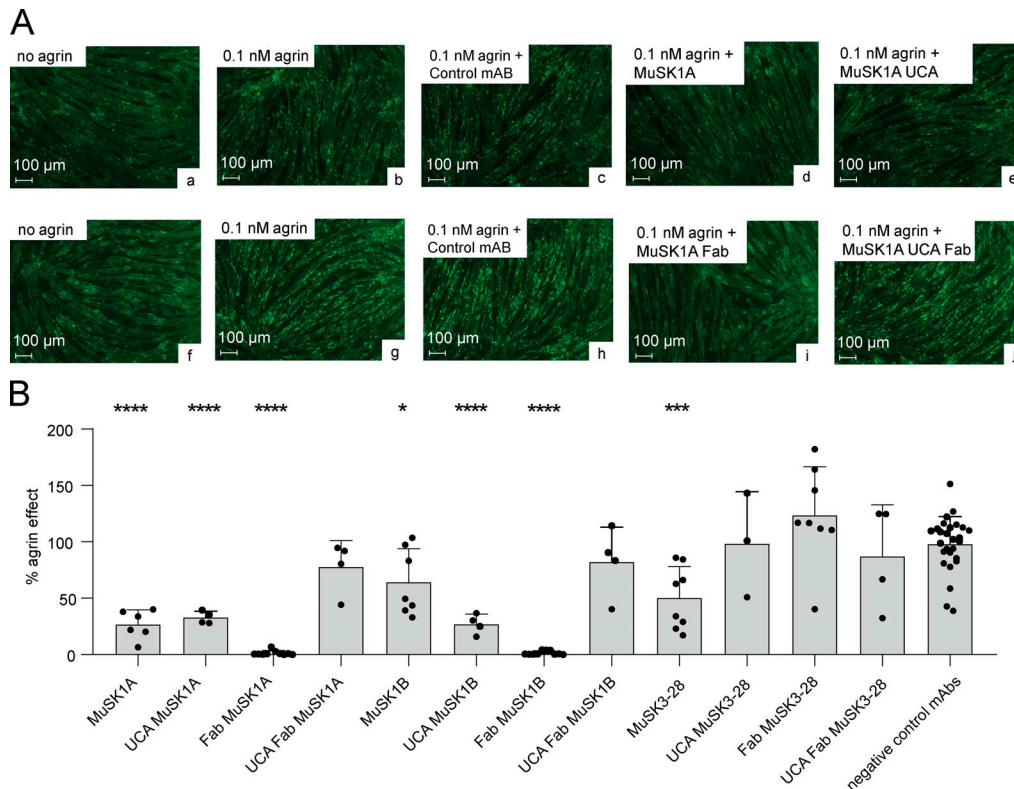


Figure 3. UCAs of MuSK autoantibodies have pathogenic capacity. AChR-clustering assay in C2C12 mouse myotubes demonstrates pathogenic capacity of MuSK mAbs. The presence of agrin in C2C12 myotube cultures leads to dense clustering of AChRs that can be readily visualized with fluorescent α -bungarotoxin and quantified. Pathogenic MuSK autoantibodies disrupt this clustering. The three different human MuSK-specific mAbs and their UCAs were tested for their ability to disrupt the AChR clustering using conditions that were previously validated (Takata et al., 2019). **(A)** Representative images (original magnification, $\times 100$) from the clustering experiments are shown. Cultured myotubes (a and f) do not show AChR clustering until agrin is added (b and g); bright spots reveal AChR clusters). The mAbs MuSK1A (d), MuSK1A UCA (e), and MuSK1A Fab (i) added at $1 \mu\text{g}/\text{ml}$ inhibit clustering. A control mAb (c and h) and the MuSK1A UCA Fab (j) do not inhibit the formation of AChR clusters. The scale bar corresponds to $100 \mu\text{m}$. **(B)** The effect of the mAb on agrin-dependent clustering was tested. Quantitative measurements of C2C12 clustering were normalized to the agrin-only effect of each individual experiment. Each data point represents the mean value of the normalized agrin effect (%) from at least three independent experiments. Bars represent the mean of means and error bars represent SDs. Multiple-comparison ANOVA with Dunnett's correction of the independent experimental data points was used to compare the effect on clustering by each mAb or Fab against the pooled results for the three human non-MuSK-specific mAbs. *, $P < 0.05$; ***, $P < 0.001$; ****, $P < 0.0001$ (only shown when significant).

process was a critical requirement for the pathogenic capacity of the monovalent Fabs. Structural data indicated that somatic mutations, which led to a large increase in binding affinity, also resulted in an increasingly negatively charged antigen-binding surface on both MuSK1A and MuSK1B. Due to the largely positively charged surface on MuSK Ig2-like domain, it is tempting to speculate that this charge complementarity contributed to the increased binding affinity. Interestingly, a reversion mutation for A25D near H CDR1 in the FR1 of MuSK3-28 largely abolished MuSK3-28 binding to MuSK in our CBA. Homology modeling of MuSK3-28 suggests that introducing this negatively charged residue during affinity maturation, which is buried in the FR region, could alter the conformation of the H CDR1 loop and may partially explain the difference in the association rate observed between the mature and UCA MuSK3-28 Fab. These collective data suggest that MuSK MG pathology occurs when a high-affinity threshold is reached by a functionally monovalent Fab-arm-exchanged IgG4.

The remarkably high affinity of these MuSK autoantibodies offers additional insight into the mechanisms of immunopathology. The affinity has only been described for a small number of pathogenic human autoantibodies; in contrast to many reported avidity measurements or estimates of avidity, which are derived from divalent mAbs. The association and dissociation rates need to be separately measured to calculate the true affinity or avidity. Measuring binding over a broad range of concentrations can give an estimate of the binding to an antigen, and as such is often used as an affinity/avidity estimate. An AChR mAb bound with an estimated avidity in the subnanomolar range (Saxena et al., 2017) and mAbs binding AQP4, derived from patients with neuromyelitis optica, have estimated avidities covering a broad range, from 24 nM to 559 nM (Cotzomi et al., 2019). The affinity measurements of a human mAb against respiratory syncytial virus (Fab19) and several reversion intermediates, together with the germline-encoded Fab, showed that SHM increased affinity and resulted in a faster association rate that was associated with an increase in antiviral

neutralizing activity (Bates et al., 2013); similar findings were described when analyzing the kinetics of antibody binding in mice (Foote and Milstein, 1991). Two of the mAbs described here have affinities for MuSK in the subnanomolar range, which was driven by a remarkably slow dissociation rate. Germline versions displayed lower affinity, which was associated with diminished pathogenicity. Thus, once these autoantibodies have engaged MuSK at the neuromuscular synapse, they may remain bound to MuSK for an extended period of time, which may be a key property of their pathology.

B cells expressing autoreactive B cell receptors (BCR) are normally eliminated from the maturing repertoire by mechanisms present at two distinct checkpoints along the B cell development pathway, thereby reducing the development of immune responses against self-antigens (Meffre and O'Connor, 2019; Wardemann et al., 2003). A number of autoimmune diseases (Cotzomi et al., 2019), including both AChR and MuSK MG (Lee et al., 2016), include defective B cell tolerance checkpoints. Consequently, in the presence of faulty counterselection, the naive repertoire includes a higher proportion of polyreactive/self-reactive B cells than found in healthy (non-autoimmune) individuals and this reservoir of polyreactive/self-reactive naive B cells may include those that bind to MuSK and thus serve as precursors to those that secrete pathogenic autoantibodies. Alternatively, B cells that escape tolerance checkpoints can be maintained in a state of clonal ignorance to protect against the development of autoimmunity; failure of clonal ignorance mechanisms may contribute to the development of autoimmunity (Aplin et al., 2003; Hannum et al., 1996; Liu et al., 2007; Pillai et al., 2011; Shlomchik et al., 1993). Given that the putative naive B cells, which were represented by the UCAs, demonstrated such high affinity for self-antigen, it is reasonable to consider that they may be clonally ignorant. Such clonally ignorant B cells can become activated without initially binding to self-antigen and then mature and generate strongly self-reactive clones that secrete pathogenic autoantibodies, such as those shown in our study.

Given that the self-antigen MuSK bound to the putative germline-encoded mAbs (experimentally approximating the BCR of naive B cell clones), it is not unreasonable to speculate that MuSK may be both initiating and driving the autoimmune response. This finding is unusual, as similar investigations of germline-encoded human mAbs demonstrate a remarkable lack of autoantigen binding that is, conversely, robust in their mature counterparts. Unmutated revertants of mAbs from patients with pemphigus vulgaris and systemic lupus erythematosus do not bind self-antigen (Di Zenzo et al., 2012; Mietzner et al., 2008; Wellmann et al., 2005). Similar patterns were found with unmutated revertants of anti-cytokine autoantibodies in autoimmune regulator (AIRE)-deficient patients (Meyer et al., 2016) and pulmonary alveolar proteinosis patients (Piccoli et al., 2015). These findings contrast with those acquired with antibodies that develop toward exogenous (nonself) antigens during a normal immune response. Examples include viral infections (Bonsignori et al., 2018; Corti et al., 2010, 2011; Pappas et al., 2014) and responses to influenza hemagglutinin, wherein unmutated revertants of virus antigen-specific mAbs, in some instances,

demonstrate binding activity. These scenarios, however, must be carefully considered, as there are some limited examples of binding by germline-reverted autoantibodies (Cho et al., 2019; Wenke et al., 2019). These collective findings may point toward the limitations of the approaches available to measure antibody-antigen interactions, including ELISAs and live CBAs, neither of which may be sufficiently sensitive to measure low-affinity interactions or accurately emulate the antigen/autoantigen binding to the BCR of naive B cells in situ, such as lymphoid tissue.

Our study is, of course, not without limitations. First, the process of producing UCA versions of mature antibodies is not absolute without having the germline B cell clone in hand. We made every effort to identify the somatic mutations harbored within the CDR3 region, including reverting the D-gene segment and using a statistical model that evaluated proposed germline configurations (Gaëta et al., 2007). Although not absolute, our reversions are as thorough as experimentally possible and thus provide the best approximate representation of the true germline BCR. However, it is possible that the UCAs do not accurately represent naive B cells from which the pathogenic clones emerged. Thus, we cannot be certain that naive B cells have the capacity to bind to MuSK and initiate the autoimmune response. The *ex vivo* isolation and characterization of rare circulating MuSK-reactive naive B cells from MG patients would be required to demonstrate that the naive repertoire harbors such autoreactive precursors. Second, we recognize that our study focused on MuSK MG and thus urge caution in generalizing our findings to include properties of IgG4 beyond this disease. Third, while the properties of the MuSK mAbs we studied were quite consistent in terms of their pathogenic capacity and UCA binding, the study of additional mAbs will be required to determine whether these characteristics are common among MuSK autoantibodies. Finally, while our data clearly demonstrate that AChR clustering was completely inhibited with the mature monovalent Fabs (MuSK1A and MuSK1B), but not inhibited with the corresponding UCA Fabs, we recognize that our measurements of clustering did not include a range of mAb concentrations. Finer quantitative differences may be revealed by testing these mAbs as such.

The collective findings of this study offer new insights into the speculative mechanism of pathogenic autoantibody production in MuSK MG. The consequence of tolerance checkpoint defects and clonal ignorance is the generation of a naive B cell repertoire populated with clones that circumvented counterselection and thus may include precursors of autoantibody-producing clones. The results of the current study suggest that the MuSK MG naive B cell repertoire may include clones capable of binding to MuSK with high affinity. We suggest that such clones may not have escaped counterselection in the presence of well-functioning B cell tolerance checkpoints or intact clonal ignorance mechanisms. Thus, these autoreactive naive B cells may initially bind to either exogenous antigens or self-antigens and participate in initiating B cell differentiation toward memory B cells and antibody-secreting cells that directly contribute to disease; alternatively, it is also possible that MuSK-specific memory B cells/antibody-secreting cells are the product of naive

B cells that do not bind to MuSK. Our study further suggests that affinity maturation may be driven by MuSK. At the stage of autoantibody production, somatic mutations are required to generate autoantibodies of extraordinarily high avidity. Fab-arm exchange then takes place, and functionally monovalent autoantibodies, which have exceeded a high-affinity threshold, bind to MuSK at the neuromuscular synapse and cause disease. Based on this model, the targeting of high-affinity antigen-specific B cells, autoantibodies, or the Fab-arm-exchange process may represent feasible therapeutic strategies for MuSK MG treatment.

Materials and methods

Autoantibody variable region site-directed mutagenesis

To identify the base changes that arose through affinity maturation process, the sequences of the MuSK mAbs were aligned against the 2018-02-24 germline reference set with IMGT/HighV-QUEST v1.6.0 (the international ImmunoGeneTics information system; [Alamyar et al., 2012](#)). We reverted the identifiable changes back to the germline-encoded UCA sequence in a step-by-step manner using the Q5 Site-Directed Mutagenesis Kit (New England BioLabs) according to the manufacturer's instructions. The primers were designed with NEBaseChanger, and 12.5 ng of plasmid was used for each individual PCR reaction (C1000 Touch Thermal Cycler; Bio-Rad). The plasmids were transformed into NEB 5- α competent *Escherichia coli* (New England BioLabs). Plasmid DNA was then isolated with the QIAprep Spin Miniprep Kit (Qiagen) and sequenced to confirm the presence of mutations.

Recombinant expression of MuSK, human mAbs, and Fabs

For crystallography, MuSK1A was expressed in Sf9 cells using the baculovirus expression system. The heavy and light chain variable domains of MuSK1A were fused to a standard human IgG1 heavy and light chain constant domain and cloned into pFastBacDual to create pBE1719. A C-terminal 6xHis-Tag was included in the heavy chain for subsequent use in purification. Sf9 cells were grown in suspension in Sf-900 II media for 3 d before harvesting. Clarified Sf9 supernatants were filtered and MuSK1A was purified by immobilized metal affinity chromatography (Ni Sepharose excel; GE Healthcare Life Sciences) followed by size-exclusion chromatography (Superdex 200 Increase 10/300 GL column) on an ÄKTA pure system in 20 mM Tris, pH 8.0, and 150 mM NaCl. Both the variable and constant domains of the light chain of MuSK1B were cloned into pCDNA3.4-TOPO vector to create pBE1779 for protein expression for crystallography of MuSK1B. The variable domain of the heavy chain of MuSK1B was fused to a standard human IgG1 CH1 constant domain and subsequently cloned into the pCDNA3.4-TOPO vector to create pBE1775. MuSK1B was then expressed from Expi293F cells transfected using ExpiFectamine with a 1:2 ratio of the corresponding heavy- (pBE1775) and light-chain plasmid (pBE1779). Culture supernatants were harvested 7 d after transfection and clarified by centrifugation. MuSK1B was purified from culture supernatants using HiTrap Protein G High Performance column (GE Healthcare Life Sciences) equilibrated

in 20 mM Tris, pH 8.0, and 150 mM NaCl. Protein was eluted in 0.1 M glycine-HCl, pH 2.5, and the pH was immediately neutralized with 1 M Tris, pH 9.0. MuSK1B was then subsequently purified using size-exclusion chromatography (Superdex 200 Increase 10/300 GL column; GE Healthcare Life Sciences) on an ÄKTA pure system in 20 mM Tris, pH 8.0, and 150 mM NaCl.

For affinity measurements, the ectodomain construct of MuSK (ectoMuSK; aa 1–472) was expressed in Sf9 cells using a baculovirus system and designed with a C-terminal Avidag and 6xHis-tag. Clarified Sf9 culture supernatants were filtered, and ectoMuSK was purified by immobilized metal affinity chromatography (HisTrap Excel; GE Healthcare Life Sciences) and exchanged into low-salt Tris-buffered saline for site-specific biotinylation. EctoMuSK was incubated with BirA in the presence of ATP, magnesium acetate, and D-biotin for 4 h at room temperature, then purified by size-exclusion chromatography (Superdex 200 Increase 10/300 GL; GE Healthcare Life Sciences).

All UCA Fab expression constructs that were used for affinity measurements and the AChR clustering assay were cloned in a pcDNA3.4-TOPO vector for expression and secretion from mammalian cells. Expi293F cells were transiently transfected using ExpiFectamine and culture supernatants were harvested 5 d post-transfection and clarified by centrifugation. Clarified Expi293F culture supernatants were filtered and Fabs were purified by successive affinity and size-exclusion chromatography (on HiTrap Protein G and Superdex 200 Increase 10/300 GL columns, respectively; GE Healthcare Life Sciences) using an ÄKTA pure system.

The mAbs were produced as previously described ([Takata et al., 2019](#)). Briefly, HEK293A were transfected with equal amounts of the heavy and the corresponding light chain plasmid using linear polyethylenimine (catalog no. 23966; Polysciences). The media was changed after 24 h to basal media (50% DMEM 12430, 50% RPMI 1640, 1% antibiotic/antimycotic, 1% Na-pyruvate, and 1% Nutridoma). After 6 d, the supernatant was harvested and Protein G Sepharose 4 Fast Flow beads (GE Healthcare Life Sciences) were used for antibody purification. For expression of mAbs using the human IgG3 constant region, a vector containing human IgG3 was purchased from Addgene (pVITRO1-102.1F10-IgG3/ λ) and then cloned into a vector for recombinant IgG expression that we previously engineered ([Ray et al., 2012](#)).

Affinity measurements

Fab binding to MuSK was measured by biolayer interferometry using an Octet RED96 system (ForteBio). Biotinylated ectoMuSK was immobilized on streptavidin coated sensors and incubated with varying concentrations of purified Fabs. During the experiment, the reaction plate was maintained at 30°C and shaken at 1,000 rpm. Data were fit using the Octet System data analysis software. After subtraction of signal from a reference sensor loaded with ectoMuSK and incubated with buffer, response curves were aligned at the equilibration step. Interstep correction was applied to align association and dissociation curves, and a Savitzky-Golay filter was applied to remove high-frequency noise. Processed association and dissociation curves were fit

globally using a 1:1 binding model to obtain kinetic constants for each Fab.

Live cell-based autoantibody assay

HEK293T (ATCC CRL3216) cells were transfected with either full-length MuSK-GFP (kindly provided by Drs. David Beeson, Angela Vincent, and Patrick Waters; University of Oxford, Oxford, UK), different ectodomain variants of MuSK-GFP (previously described in [Takata et al., 2019](#)) or the AChR domains (2 α , β , δ , and ϵ) together with Rapsyn-GFP (kindly provided by Drs. David Beeson, Angela Vincent, and Patrick Waters). On the day of the CBA, the antibodies were added to the transfected cells in either a dilution series (10–0.02 μ g/ml) or at a concentration of 10, 1, or 0.1 μ g/ml. For the epitope determination assay, all constructs were measured at 10 μ g/ml. The binding of each mAb was detected with Alexa Fluor-conjugated AffiniPure Rabbit Anti-Human IgG, Fc γ (309-605-008; Jackson ImmunoResearch) on a BD LSRFortessa (BD Biosciences). FlowJo software was used for analysis.

Crystallization and structure determination

Gel filtration fractions containing purified MuSK1A were concentrated to 10 mg/ml. MuSK1A crystals were grown at 18°C by vapor diffusion and after ~4 d grew from drops consisting of 100 nl protein plus 100 nl of a reservoir solution consisting of 20% wt/vol polyethylene glycol (PEG) 6K (Precipitant) and 0.1 M Bicine 8.5 pH (Buffer) from the JCSG Core I (Qiagen) screen. Reservoir solution was supplemented with 15% ethylene glycol for cryoprotection. Gel filtration fractions containing purified MuSK1B were concentrated to 10 mg/ml. MuSK1B crystals grew after 1 d at 18°C by vapor diffusion from drops consisting of 100 nl protein plus 100 nl of a reservoir solution consisting of 0.085 M Hepes, pH 7.5, 17% PEG 4K, 8.5% isopropyl alcohol, and 15% glycerol from the JCSG Core II (Qiagen) screen. Reservoir solution was supplemented with 5% glycerol for cryoprotection. For both MuSK1A and MuSK1B, native diffraction data were collected at National Institute of General Medical Sciences/National Cancer Institute-Collaborative Access Team (GM/CA-CAT) beamline 23-ID-B at the Advanced Photon Source and reduced using XDS (Table S2; [Kabsch, 2010](#)). MuSK1A was indexed to P2₁, and MuSK1B was indexed to P2₁2₁2₁. Crystallographic data quality was assessed for outliers and the potential presence of twinning using Xtriage ([Zwart et al., 2005](#)), and the high-resolution limit of each dataset was assessed using CC1/2 and cut where this metric dropped below ~50% in the highest-resolution shell, corresponding to CC* values of 0.725 and 0.781 for the MuSK1A and MuSK1B models, respectively, after refinement ([Karpplus and Diederichs, 2012](#)). The MuSK1A asymmetric unit consists of two sets of MuSK1A Fabs, and MuSK1A was phased by molecular replacement using Phaser ([McCoy et al., 2007](#)), first using the Fab constant domains from PDB code 6DW2 as a search model and then using the Fab variable domains from 6DW2 as a search model. MuSK1B has one Fab in the asymmetric unit, and molecular replacement was performed using the autoMR module from Phaser. First, the Fab constant domains from PDB code 7FAB were used as a search model, followed by the Fab variable domains from PDB code

8FAB. The resulting models were adjusted in Coot ([Emsley et al., 2010](#)) and refined using Phenix ([Afonine et al., 2013, 2018](#); [Liebschner et al., 2019](#)). Protein models were validated using MolProbity ([Williams et al., 2018](#)).

Polyreactivity ELISA

Recombinant IgG was tested for polyreactivity on microplates coated with 20 μ g/ml dsDNA, 10 μ g/ml LPS, or 15 μ g/ml recombinant human insulin (all purchased from Sigma-Aldrich) using a previously described approach ([Wardemann et al., 2003](#)). The highly polyreactive antibody ED38 was used as a positive control ([Sng et al., 2019](#)). All antibodies and the control were added in a dilution series (1 μ g/ml, 0.25 μ g/ml, 0.063 μ g/ml, and 0.016 μ g/ml). The HRP Substrate Kit (Bio-Rad) was used to develop the ELISA. Absorbance of the wells were recorded with a PowerWave XS (BIO-TEK) microplate reader.

AChR clustering assay

The C2C12 AChR clustering assay was performed as reported ([Takata et al., 2019](#)). Briefly, C2C12 mouse myoblasts (ATCC) were cultured in growth medium (DMEM 11960; Thermo Fisher Scientific), 10% FBS (Gibco), 1% penicillin/streptomycin (Gibco), and 1% L-glutamine (Gibco). After three passages, C2C12 cells were plated in 24-well plates (100,000 cells/well) and grown until a confluence of 90–95% was reached. To differentiate the cells, the media was changed to differentiation medium (DMEM 12430; Thermo Fisher Scientific), 2% FBS, 1% penicillin/streptomycin (Gibco), and 1 μ M insulin (Sigma-Aldrich). The differentiation media was changed daily until fusion was evident (36–48 h). AChR clustering was induced for 14–16 h with 0.1 nM agrin (R&D Systems). mAbs or Fabs were added at the previously established concentration of 1 μ g/ml (6.7 nM) together with agrin or alone ([Takata et al., 2019](#)). After the induction of AChR clustering, AChRs were visualized through the application of 1 μ g/ml Alexa Fluor 647-labeled α -bungarotoxin (Invitrogen) for 1 h at 37°C. After staining, cells were washed twice with medium (5 min at 37°C) and fixed with 3% paraformaldehyde/paraformaldehyde for 20 min at room temperature. Duplicate wells, for each condition, were used to perform technical replicates; between four and eight randomly chosen visual fields were captured for every condition. AChR clusters were counted using ImageJ software, and the mean of the clusters per visual field, per condition was calculated. Experiments were performed independently, at least three times, to produce biological replicates. AChR clusters were normalized for the effect of agrin in each experiment. Reported results are from experiments in which a minimum threefold effect of agrin-induced clustering over the baseline was observed.

Statistics

Statistical significance was assessed with Prism Software (GraphPad version 8.0) by multiple-comparison ANOVA with Dunnett's correction for AChR clustering in the C2C12 assay as well as for the light chain contribution to binding. Welch's *t* test was used to evaluate the statistical difference in inhibiting AChR clustering between UCA and corresponding mature Fabs.

Online supplemental material

Fig. S1 shows the results from testing the intermediates of MuSK1A, MuSK1B, and MuSK3-28 mAbs with the MuSK CBA and the data from the mutagenesis analysis of AChR-specific mAb 637 with an AChR CBA. **Fig. S2** shows the results of the MuSK domain binding of all three mAbs and their UCA counterparts with a CBA expressing several MuSK-GFP domain variants. **Fig. S3** shows the reactivity of the mature and UCA mAbs against LPS, dsDNA, and insulin as tested by ELISA. **Fig. S4** shows the biolayer interferometry curves related to the affinity measurements of the mature and UCA Fabs to MuSK. **Fig. S5** compares the structure of the MuSK1A and MuSK1B Fabs to sequence-related Fabs. Table S1 shows the molecular characteristics of the MuSK-specific mAbs MuSK1A, MuSK1B, and MuSK3-28. Table S2 provides additional crystallographic data and refinement statistics.

Acknowledgments

The authors thank Karen Boss for providing editorial assistance.

This project was supported by the National Institute of Allergy and Infectious Diseases of the National Institutes of Health through grant awards to K.C. O'Connor (award numbers R01-AI114780 and R21-AI142198) and through the Rare Diseases Clinical Research Consortia of the National Institutes of Health (award number U54-NS115054), a Neuromuscular Disease Research program award from the Muscular Dystrophy Association to K.C. O'Connor (award number MDA575198), and a "pilot" and "transformational" grant from the Colton Center for Autoimmunity to D.C. Ekiert and S.J. Burden. M.L. Fichtner is supported by a Brown-Coxe fellowship. P. Stathopoulos was partly supported by the Onassis Foundation under the Special Grant and Support Program for Scholars' Association Members (R ZO 006/2018-2019).

Author contributions: This study was originally conceived, initiated, and directed by K.C. O'Connor. M.L. Fichtner led the laboratory work at Yale, designing, executing, and interpreting experiments associated with the mutagenesis, mAb expression, C2C12 assay, and the CBA and directed P.A. Suarez in performing and validating the mutagenesis and expressing the mAb variants. P. Stathopoulos provided assistance with experimental design and data interpretation associated with the C2C12 assay and CBAs. D.C. Ekiert and C. Vieni planned, designed, and executed the crystal structures. C. Vieni, L. Kolich, and R.L. Redler produced the Fabs and executed the affinity measurements. K. Takata helped design and execute the mutagenesis and CBAs. P.A. Suarez assisted with C2C12 measurements. R. Jiang executed the bioinformatic analyses. D.C. Ekiert and S.J. Burden provided key contributions to the overall project scope and experimental design and directed the laboratory work at New York University. R.J. Nowak provided the clinical specimens from which the mAb were derived and provided insight on the clinical and therapeutic relevance of the findings. The manuscript was initially drafted by M.L. Fichtner and K.C. O'Connor. The graphical abstract was created with BioRender.com by M.L. Fichtner. All authors contributed to the editing and revising of the manuscript.

Disclosures: M.L. Fichtner reported grants from Grifols outside the submitted work. P. Stathopoulos reported grants from

Onassis Foundation outside the submitted work. R.J. Nowak reported no conflicts directly related to this work. R.J. Nowak had received research support from Alexion, argenx, Ra Pharma, Momenta, Genentech, Immunovant, and Viela Bio related to the conduct of clinical trials for myasthenia gravis. K.C. O'Connor reported grants from Ra Pharma and personal fees from Alexion outside the submitted work; and received research support from Ra Pharma and is a consultant and equity shareholder of Cabaletta Bio. K.C. O'Connor is the recipient of a sponsored research subaward from the University of Pennsylvania, the primary financial sponsor of which is Cabaletta Bio. No other disclosures were reported.

Submitted: 17 March 2020

Revised: 4 June 2020

Accepted: 16 July 2020

References

- Aalberse, R.C., S.O. Stapel, J. Schuurman, and T. Rispens. 2009. Immunoglobulin G4: an odd antibody. *Clin. Exp. Allergy*. 39:469–477. <https://doi.org/10.1111/j.1365-2222.2009.03207.x>
- Afonine, P.V., R.W. Grosse-Kunstleve, P.D. Adams, and A. Urzhumtsev. 2013. Bulk-solvent and overall scaling revisited: faster calculations, improved results. *Acta Crystallogr. D Biol. Crystallogr.* 69:625–634. <https://doi.org/10.1107/S0907444913000462>
- Afonine, P.V., B.K. Poon, R.J. Read, O.V. Sobolev, T.C. Terwilliger, A. Urzhumtsev, and P.D. Adams. 2018. Real-space refinement in PHENIX for cryo-EM and crystallography. *Acta Crystallogr. D Struct. Biol.* 74:531–544. <https://doi.org/10.1107/S2059798318006551>
- Alamyar, E., P. Duroux, M.P. Lefranc, and V. Giudicelli. 2012. IMGT[®] tools for the nucleotide analysis of immunoglobulin (IG) and T cell receptor (TR) V-(D)-J repertoires, polymorphisms, and IG mutations: IMGT/V-QUEST and IMGT/HighV-QUEST for NGS. *Methods Mol. Biol.* 882: 569–604. https://doi.org/10.1007/978-1-61779-842-9_32
- Aplin, B.D., C.L. Keech, A.L. de Kauwe, T.P. Gordon, D. Cavill, and J. McCluskey. 2003. Tolerance through indifference: autoreactive B cells to the nuclear antigen La show no evidence of tolerance in a transgenic model. *J. Immunol.* 171:5890–5900. <https://doi.org/10.4049/jimmunol.171.11.5890>
- Bates, J.T., C.J. Keefer, T.J. Utey, B.E. Correia, W.R. Schief, and J.E. Crowe, Jr. 2013. Reversion of somatic mutations of the respiratory syncytial virus-specific human monoclonal antibody Fab19 reveal a direct relationship between association rate and neutralizing potency. *J. Immunol.* 190: 3732–3739. <https://doi.org/10.4049/jimmunol.1202964>
- Bennett, J.L., C. Lam, S.R. Kalluri, P. Saikali, K. Bautista, C. Dupree, M. Glogowska, D. Case, J.P. Antel, G.P. Owens, et al. 2009. Intrathecal pathogenic anti-aquaporin-4 antibodies in early neuromyelitis optica. *Ann. Neurol.* 66:617–629. <https://doi.org/10.1002/ana.21802>
- Blom, N., T. Sicheritz-Pontén, R. Gupta, S. Gammeltoft, and S. Brunak. 2004. Prediction of post-translational glycosylation and phosphorylation of proteins from the amino acid sequence. *Proteomics*. 4:1633–1649. <https://doi.org/10.1002/pmic.200300771>
- Bonsignori, M., E. Scott, K. Wiehe, D. Easterhoff, S.M. Alam, K.K. Hwang, M. Cooper, S.M. Xia, R. Zhang, D.C. Montefiori, et al. 2018. Inference of the HIV-1 VRC01 Antibody Lineage Unmutated Common Ancestor Reveals Alternative Pathways to Overcome a Key Glycan Barrier. *Immunity*. 49: 1162–1174.e8. <https://doi.org/10.1016/j.immuni.2018.10.015>
- Cho, A., A.L. Caldara, N.A. Ran, Z. Menne, R.C. Kauffman, M. Affer, A. Llovret, C. Norwood, A. Scanlan, G. Mantus, et al. 2019. Single-Cell Analysis Suggests that Ongoing Affinity Maturation Drives the Emergence of Pemphigus Vulgaris Autoimmune Disease. *Cell Rep.* 28:909–922.e6. <https://doi.org/10.1016/j.celrep.2019.06.066>
- Corti, D., A.L. Suguitan, Jr., D. Pinna, C. Silacci, B.M. Fernandez-Rodriguez, F. Vanzetta, C. Santos, C.J. Luke, F.J. Torres-Velez, N.J. Temperton, et al. 2010. Heterosubtypic neutralizing antibodies are produced by individuals immunized with a seasonal influenza vaccine. *J. Clin. Invest.* 120:1663–1673. <https://doi.org/10.1172/JCI41902>
- Corti, D., J. Voss, S.J. Gamblin, G. Codoni, A. Macagno, D. Jarrossay, S.G. Vachieri, D. Pinna, A. Minola, F. Vanzetta, et al. 2011. A neutralizing

- antibody selected from plasma cells that binds to group 1 and group 2 influenza A hemagglutinins. *Science*. 333:850–856. <https://doi.org/10.1126/science.1205669>
- Cotzomi, E., P. Stathopoulos, C.S. Lee, A.M. Ritchie, J.N. Soltys, F.R. Delmotte, T. Oe, J. Sng, R. Jiang, A.K. Ma, et al. 2019. Early B cell tolerance defects in neuromyelitis optica favour anti-AQP4 autoantibody production. *Brain*. 142:1598–1615. <https://doi.org/10.1093/brain/awz106>
- Di Zenzo, G., G. Di Lullo, D. Corti, V. Calabresi, A. Sinistro, F. Vanzetta, B. Didona, G. Cianchini, M. Hertl, R. Eming, et al. 2012. Pemphigus autoantibodies generated through somatic mutations target the desmoglein-3 cis-interface. *J. Clin. Invest.* 122:3781–3790. <https://doi.org/10.1172/JCI64413>
- Emsley, P., B. Lohkamp, W.G. Scott, and K. Cowtan. 2010. Features and development of Coot. *Acta Crystallogr. D Biol. Crystallogr.* 66:486–501. <https://doi.org/10.1107/S0907444910007493>
- Foote, J., and C. Milstein. 1991. Kinetic maturation of an immune response. *Nature*. 352:530–532. <https://doi.org/10.1038/352530a0>
- Gaëta, B.A., H.R. Malming, K.J. Jackson, M.E. Bain, P. Wilson, and A.M. Collins. 2007. iHMMune-align: hidden Markov model-based alignment and identification of germline genes in rearranged immunoglobulin gene sequences. *Bioinformatics*. 23:1580–1587. <https://doi.org/10.1093/bioinformatics/btm147>
- Gilhus, N.E.. 2016. Myasthenia Gravis. *N. Engl. J. Med.* 375:2570–2581. <https://doi.org/10.1056/NEJMra1602678>
- Graus, Y.F., M.H. de Baets, P.W. Parren, S. Berrih-Aknin, J. Wokke, P.J. van Breda Vriesman, and D.R. Burton. 1997. Human anti-nicotinic acetylcholine receptor recombinant Fab fragments isolated from thymus-derived phage display libraries from myasthenia gravis patients reflect predominant specificities in serum and block the action of pathogenic serum antibodies. *J. Immunol.* 158:1919–1929.
- Hannum, L.G., D. Ni, A.M. Haberman, M.G. Weigert, and M.J. Shlomchik. 1996. A disease-related rheumatoid factor autoantibody is not tolerized in a normal mouse: implications for the origins of autoantibodies in autoimmune disease. *J. Exp. Med.* 184:1269–1278. <https://doi.org/10.1084/jem.184.4.1269>
- Herbst, R., and S.J. Burden. 2000. The juxtamembrane region of MuSK has a critical role in agrin-mediated signaling. *EMBO J.* 19:67–77. <https://doi.org/10.1093/emboj/19.1.67>
- Hoch, W., J. McConville, S. Helms, J. Newsom-Davis, A. Melms, and A. Vincent. 2001. Auto-antibodies to the receptor tyrosine kinase MuSK in patients with myasthenia gravis without acetylcholine receptor antibodies. *Nat. Med.* 7:365–368. <https://doi.org/10.1038/85520>
- Huijbers, M.G., W. Zhang, R. Klooster, E.H. Niks, M.B. Friese, K.R. Straasheijm, P.E. Thijssen, H. Vrolijk, J.J. Plomp, P. Vogels, et al. 2013. MuSK IgG4 autoantibodies cause myasthenia gravis by inhibiting binding between MuSK and Lrp4. *Proc. Natl. Acad. Sci. USA*. 110:20783–20788. <https://doi.org/10.1073/pnas.1313944110>
- Huijbers, M.G., D.L. Vergoossen, Y.E. Fillié-Grijpma, I.E. van Es, M.T. Koning, L.M. Slot, H. Veelken, J.J. Plomp, S.M. van der Maarel, and J.J. Verschuuren. 2019. MuSK myasthenia gravis monoclonal antibodies: Valency dictates pathogenicity. *Neurol. Neuroimmunol. Neuroinflamm.* 6. e547. <https://doi.org/10.1212/NXI.0000000000000547>
- Kabsch, W.. 2010. XDS. *Acta Crystallogr. D Biol. Crystallogr.* 66:125–132. <https://doi.org/10.1107/S0907444909047337>
- Karplus, P.A., and K. Diederichs. 2012. Linking crystallographic model and data quality. *Science*. 336:1030–1033. <https://doi.org/10.1126/science.1218231>
- Koers, J., N.I.L. Derksen, P. Ooijevaar-de Heer, B. Nota, F.S. van de Bovenkamp, G. Vidarsson, and T. Rispens. 2019. Biased N-Glycosylation Site Distribution and Acquisition across the Antibody V Region during B Cell Maturation. *J. Immunol.* 202:2220–2228. <https://doi.org/10.4049/jimmunol.1801622>
- Koneczny, I., J.A. Stevens, A. De Rosa, S. Huda, M.G. Huijbers, A. Saxena, M. Maestri, K. Lazaridis, P. Zisimopoulou, S. Tzartos, et al. 2017. IgG4 autoantibodies against muscle-specific kinase undergo Fab-arm exchange in myasthenia gravis patients. *J. Autoimmun.* 77:104–115. <https://doi.org/10.1016/j.jaut.2016.11.005>
- Lee, J.Y., P. Stathopoulos, S. Gupta, J.M. Bannock, R.J. Barohn, E. Cotzomi, M.M. Dimachkie, L. Jacobson, C.S. Lee, H. Morbach, et al. 2016. Compromised fidelity of B-cell tolerance checkpoints in AChR and MuSK myasthenia gravis. *Ann. Clin. Transl. Neurol.* 3:443–454. <https://doi.org/10.1002/acn3.311>
- Liebschner, D., P.V. Afonine, M.L. Baker, G. Bunkóczi, V.B. Chen, T.I. Croll, B. Hintze, L.W. Hung, S. Jain, A.J. McCoy, et al. 2019. Macromolecular structure determination using X-rays, neutrons and electrons: recent developments in Phenix. *Acta Crystallogr. D Struct. Biol.* 75:861–877. <https://doi.org/10.1107/S2059798319011471>
- Liu, X., L.J. Wysoccki, and T. Manser. 2007. Autoantigen-B cell antigen receptor interactions that regulate expression of B cell antigen receptor Loci. *J. Immunol.* 178:5035–5047. <https://doi.org/10.4049/jimmunol.178.8.5035>
- McCoy, A.J., R.W. Grosse-Kunstleve, P.D. Adams, M.D. Winn, L.C. Storoni, and R.J. Read. 2007. Phaser crystallographic software. *J. Appl. Cryst.* 40: 658–674. <https://doi.org/10.1107/S0021889807021206>
- Meffre, E., and K.C. O'Connor. 2019. Impaired B-cell tolerance checkpoints promote the development of autoimmune diseases and pathogenic autoantibodies. *Immunol. Rev.* 292:90–101. <https://doi.org/10.1111/imr.12821>
- Meyer, S., M. Woodward, C. Hertel, P. Vlaicu, Y. Haque, J. Kärner, A. Macagno, S.C. Onooha, D. Fishman, H. Peterson, et al; APECED patient collaborative. 2016. AIRE-Deficient Patients Harbor Unique High-Affinity Disease-Ameliorating Autoantibodies. *Cell*. 166:582–595. <https://doi.org/10.1016/j.cell.2016.06.024>
- Mietzner, B., M. Tsuiji, J. Scheid, K. Velinon, T. Tiller, K. Abraham, J.B. Gonzalez, V. Pascual, D. Stichweh, H. Wardemann, et al. 2008. Autoreactive IgG memory antibodies in patients with systemic lupus erythematosus arise from nonreactive and polyreactive precursors. *Proc. Natl. Acad. Sci. USA*. 105:9727–9732. <https://doi.org/10.1073/pnas.0803644105>
- Neuberger, M.S.. 2002. Novartis Medal Lecture. Antibodies: a paradigm for the evolution of molecular recognition. *Biochem. Soc. Trans.* 30:341–350. <https://doi.org/10.1042/bst0300341>
- Niks, E.H., Y. van Leeuwen, M.I. Leite, F.W. Dekker, A.R. Wintzen, P.W. Wirtz, A. Vincent, M.J. van Tol, C.M. Jol-van der Zijde, and J.J. Verschuuren. 2008. Clinical fluctuations in MuSK myasthenia gravis are related to antigen-specific IgG4 instead of IgG1. *J. Neuroimmunol.* 195: 151–156. <https://doi.org/10.1016/j.jneuroim.2008.01.013>
- Pappas, L., M. Foglierini, L. Piccoli, N.L. Kallewaard, F. Turrini, C. Silacci, B. Fernandez-Rodriguez, G. Agatic, I. Giacchetto-Sasselli, G. Pellicciotta, et al. 2014. Rapid development of broadly influenza neutralizing antibodies through redundant mutations. *Nature*. 516:418–422. <https://doi.org/10.1038/nature13764>
- Piccoli, L., I. Campo, C.S. Fregni, B.M. Rodriguez, A. Minola, F. Sallusto, M. Luisetti, D. Corti, and A. Lanzavecchia. 2015. Neutralization and clearance of GM-CSF by autoantibodies in pulmonary alveolar proteinosis. *Nat. Commun.* 6:7375. <https://doi.org/10.1038/ncomms8375>
- Pillai, S., H. Mattoo, and A. Cariappa. 2011. B cells and autoimmunity. *Curr. Opin. Immunol.* 23:721–731. <https://doi.org/10.1016/j.coi.2011.10.007>
- Rajewsky, K.. 1996. Clonal selection and learning in the antibody system. *Nature*. 381:751–758. <https://doi.org/10.1038/381751a0>
- Ray, A., A.A. Amato, E.M. Bradshaw, K.J. Felice, D.B. DiCapua, J.M. Goldstein, I.E. Lundberg, R.J. Nowak, H.L. Ploegh, E. Spooner, et al. 2012. Autoantibodies produced at the site of tissue damage provide evidence of humoral autoimmunity in inclusion body myositis. *PLoS One*. 7. e46709. <https://doi.org/10.1371/journal.pone.0046709>
- Sarvas, H., and O. Mäkelä. 1970. Haptenated bacteriophage in the assay of antibody quantity and affinity: maturation of an immune response. *Immunochemistry*. 7:933–943. [https://doi.org/10.1016/0019-2791\(70\)90054-6](https://doi.org/10.1016/0019-2791(70)90054-6)
- Saxena, A., J. Stevens, H. Cetin, I. Koneczny, R. Webster, K. Lazaridis, S. Tzartos, K. Vrolix, G. Nogaes-Gadea, B. Machiels, et al. 2017. Characterization of an anti-fetal AChR monoclonal antibody isolated from a myasthenia gravis patient. *Sci. Rep.* 7:14426. <https://doi.org/10.1038/s41598-017-14350-8>
- Shlomchik, M.J., D. Zharhary, T. Saunders, S.A. Camper, and M.G. Weigert. 1993. A rheumatoid factor transgenic mouse model of autoantibody regulation. *Int. Immunol.* 5:1329–1341. <https://doi.org/10.1093/intimm/5.10.1329>
- Sng, J., B. Ayoglu, J.W. Chen, J.-N. Schickel, E.M.N. Ferre, S. Glauzy, N. Romberg, M. Hoening, C. Cunningham-Rundles, P.J. Utz, et al. 2019. AIRE expression controls the peripheral selection of autoreactive B cells. *Sci. Immunol.* 4. eaav6778. <https://doi.org/10.1126/sciimmunol.aav6778>
- Stathopoulos, P., A. Kumar, R.J. Nowak, and K.C. O'Connor. 2017. Autoantibody-producing plasmablasts after B cell depletion identified in muscle-specific kinase myasthenia gravis. *JCI Insight*. 2. e94263. <https://doi.org/10.1172/jci.insight.94263>
- Stiegler, A.L., S.J. Burden, and S.R. Hubbard. 2006. Crystal structure of the agrin-responsive immunoglobulin-like domains 1 and 2 of the receptor tyrosine kinase MuSK. *J. Mol. Biol.* 364:424–433. <https://doi.org/10.1016/j.jmb.2006.09.019>

- Takata, K., P. Stathopoulos, M. Cao, M. Mané-Damas, M.L. Fichtner, E.S. Benotti, L. Jacobson, P. Waters, S.R. Irani, P. Martinez-Martinez, et al. 2019. Characterization of pathogenic monoclonal autoantibodies derived from muscle-specific kinase myasthenia gravis patients. *JCI Insight*. 4. e127167. <https://doi.org/10.1172/jci.insight.127167>
- van de Bovenkamp, F.S., L. Hafkenscheid, T. Rispens, and Y. Rombouts. 2016. The Emerging Importance of IgG Fab Glycosylation in Immunity. *J. Immunol.* 196:1435–1441. <https://doi.org/10.4049/jimmunol.1502136>
- van de Bovenkamp, F.S., N.I.L. Derksen, P. Ooijselaar-de Heer, K.A. van Schie, S. Kruithof, M.A. Berkowska, C.E. van der Schoot, H. Ijspeert, M. van der Burg, A. Gils, et al. 2018. Adaptive antibody diversification through N-linked glycosylation of the immunoglobulin variable region. *Proc. Natl. Acad. Sci. USA*. 115:1901–1906. <https://doi.org/10.1073/pnas.1711720115>
- van der Neut Kolfschoten, M., J. Schuurman, M. Losen, W.K. Bleeker, P. Martinez-Martinez, E. Vermeulen, T.H. den Bleker, L. Wiegman, T. Vink, L.A. Aarden, et al. 2007. Anti-inflammatory activity of human IgG4 antibodies by dynamic Fab arm exchange. *Science*. 317:1554–1557. <https://doi.org/10.1126/science.1144603>
- Vincent, A.. 2002. Unravelling the pathogenesis of myasthenia gravis. *Nat. Rev. Immunol.* 2:797–804. <https://doi.org/10.1038/nri916>
- Vincent, A., D. Beeson, and B. Lang. 2000. Molecular targets for autoimmune and genetic disorders of neuromuscular transmission. *Eur. J. Biochem.* 267:6717–6728. <https://doi.org/10.1046/j.1432-1033.2000.01785.x>
- Wardemann, H., S. Yurasov, A. Schaefer, J.W. Young, E. Meffre, and M.C. Nussenzweig. 2003. Predominant autoantibody production by early human B cell precursors. *Science*. 301:1374–1377. <https://doi.org/10.1126/science.1086907>
- Wellmann, U., M. Letz, M. Herrmann, S. Angermüller, J.R. Kalden, and T.H. Winkler. 2005. The evolution of human anti-double-stranded DNA autoantibodies. *Proc. Natl. Acad. Sci. USA*. 102:9258–9263. <https://doi.org/10.1073/pnas.0500132102>
- Wenke, N.K., J. Kreye, E. Andrzejak, A. van Casteren, J. Leubner, M.S. Murgueitio, S.M. Reincke, C. Secker, L. Schmidl, C. Geis, et al. 2019. N-methyl-D-aspartate receptor dysfunction by unmutated human antibodies against the NR1 subunit. *Ann. Neurol.* 85:771–776. <https://doi.org/10.1002/ana.25460>
- Williams, C.J., J.J. Headd, N.W. Moriarty, M.G. Prisant, L.L. Videau, L.N. Deis, V. Verma, D.A. Keedy, B.J. Hintze, V.B. Chen, et al. 2018. MolProbity: More and better reference data for improved all-atom structure validation. *Protein Sci.* 27:293–315. <https://doi.org/10.1002/pro.3330>
- Zwart PH, R. W. Grosse-Kunstleve, P.D. Adams. 2005. Xtriage and Fest: automatic assessment of x-ray data and substructure structure factor estimation. *CCP4 Newsletter*. 43:99–107.

Supplemental material

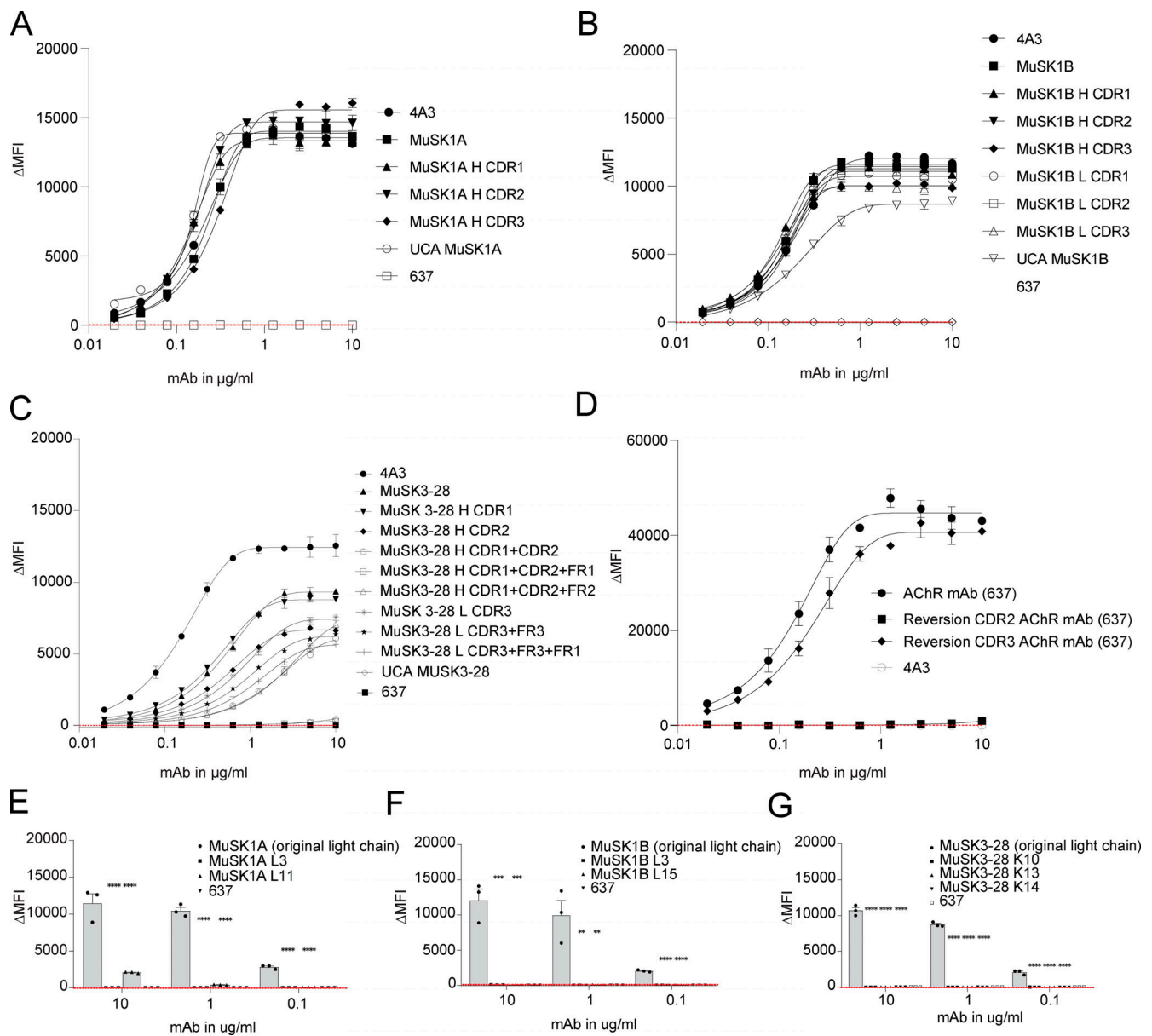


Figure S1. Intermediates of MuSK1A, MuSK1B, and MuSK3-28 bind to the MuSK autoantigen and the light chains make contributions to binding. MuSK-specific mAbs were tested for surface binding to MuSK on MuSK-GFP-transfected human embryonic kidney (HEK) cells, and AChR-specific mAbs were tested for surface binding to AChR on AChR Rapsyn-GFP-transfected HEK cells. The mutated regions of each intermediate construct are indicated by adding either the heavy (H) or light (L) chain to the name of the construct, together with the regions that were mutated. **(A–D)** Binding to MuSK (A–C) and AChR (D) was tested over 10 twofold serial dilutions of MuSK1A (A), MuSK1B (B), MuSK 3–28 (C), and AChR-specific mAb 637 (D) ranging from 10 to 0.02 $\mu\text{g/ml}$. Humanized MuSK mAb 4A3 was used as the positive control and AChR-specific mAb 637 as the negative control. **(E–G)** The variable light chain (VL) of the endogenous VH–VL pair was replaced to test the VL contributions to binding. All three mature mAbs—MuSK1A (E), MuSK1B (F), and MuSK3-28 (G)—were paired with light chains from different subtypes consistent with their subclass and recombinantly expressed. These newly generated mAbs were tested for their binding capacity by CBA. AChR-specific mAb 637 was used as the negative control. The ΔMFI was calculated by subtracting the signal from nontransfected cells from the signal of transfected cells. Each data point or bar graph represents the mean value from two (A–D) to three (E and F) independent experiments, and error bars represent SDs. Values greater than the mean + four SDs of the negative mAb at 1.25 $\mu\text{g/ml}$ (indicated by the horizontal dotted line) were considered positive. Statistical differences are shown when significant (multiple-comparisons ANOVA against the pooled results of the endogenous heavy- and light-chain combination with Dunnett’s correction; **, $P < 0.01$; ***, $P < 0.001$; ****, $P < 0.0001$).

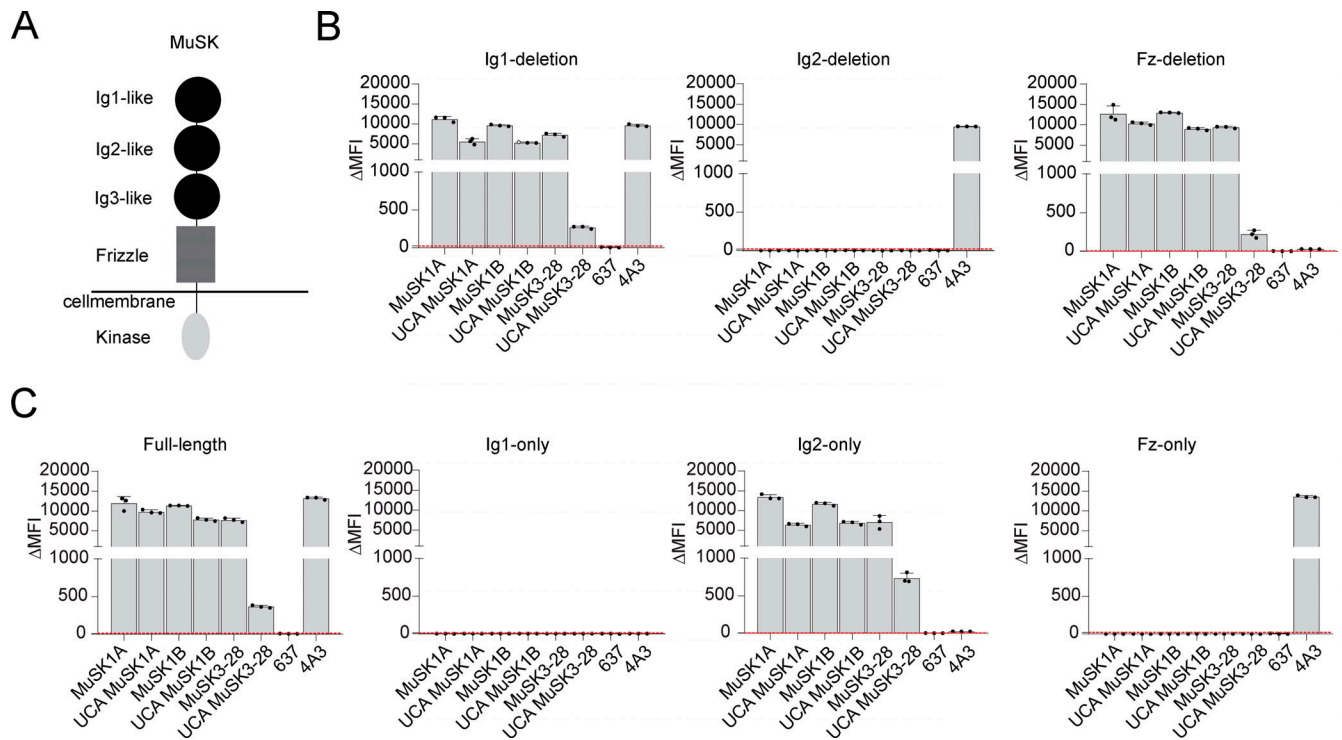


Figure S2. **Mature MuSK mAbs and their UCA counterparts bind to the same MuSK domain.** The MuSK mAbs and the UCA were tested for domain binding and recognition with a CBA expressing MuSK-GFP domain variants. **(A)** Illustration of the full-length MuSK receptor. **(B and C)** The ectodomain of MuSK consists of several different Ig-like domains and a frizzle domain. Different mutations of the MuSK protein consisting of a domain deletion or specific domain-only construct were tested for binding by the mAbs. Humanized MuSK mAb 4A3 was used as the positive control and AChR-specific mAb 637 as the negative control. Results for each mAb are shown. The Δ MFI was calculated by subtracting the signal from nontransfected cells from the signal of transfected cells. Each bar graph represents the mean value from three independent experiments. Bars represent means and error bars represent SDs. Values greater than the mean + four SDs of the negative mAb 637, indicated by horizontal dotted lines, were considered positive.

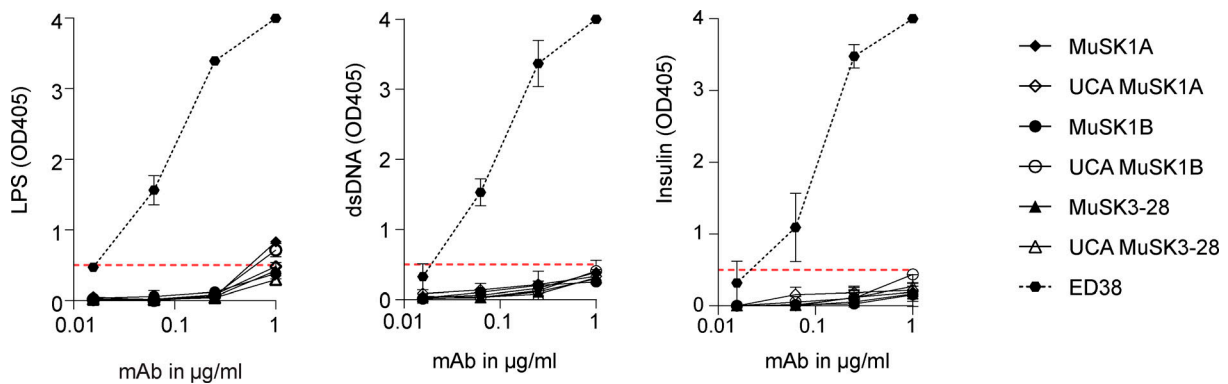


Figure S3. **Mature and UCA MuSK mAbs are not polyreactive.** The reactivity of the mature and UCA mAbs against LPS (A), dsDNA (B) and insulin (C) was tested by ELISA. ED38, a mAb cloned from a VpreB + L + peripheral B cell, was used as a positive control and shown by the dotted line curves. Each data point represents the mean value of two independent experiments, and the error bars represent SDs. Solid line curves represent MuSK mAbs and the UCAs. Dotted horizontal red lines mark the positive reactivity cutoff at OD405 0.5.

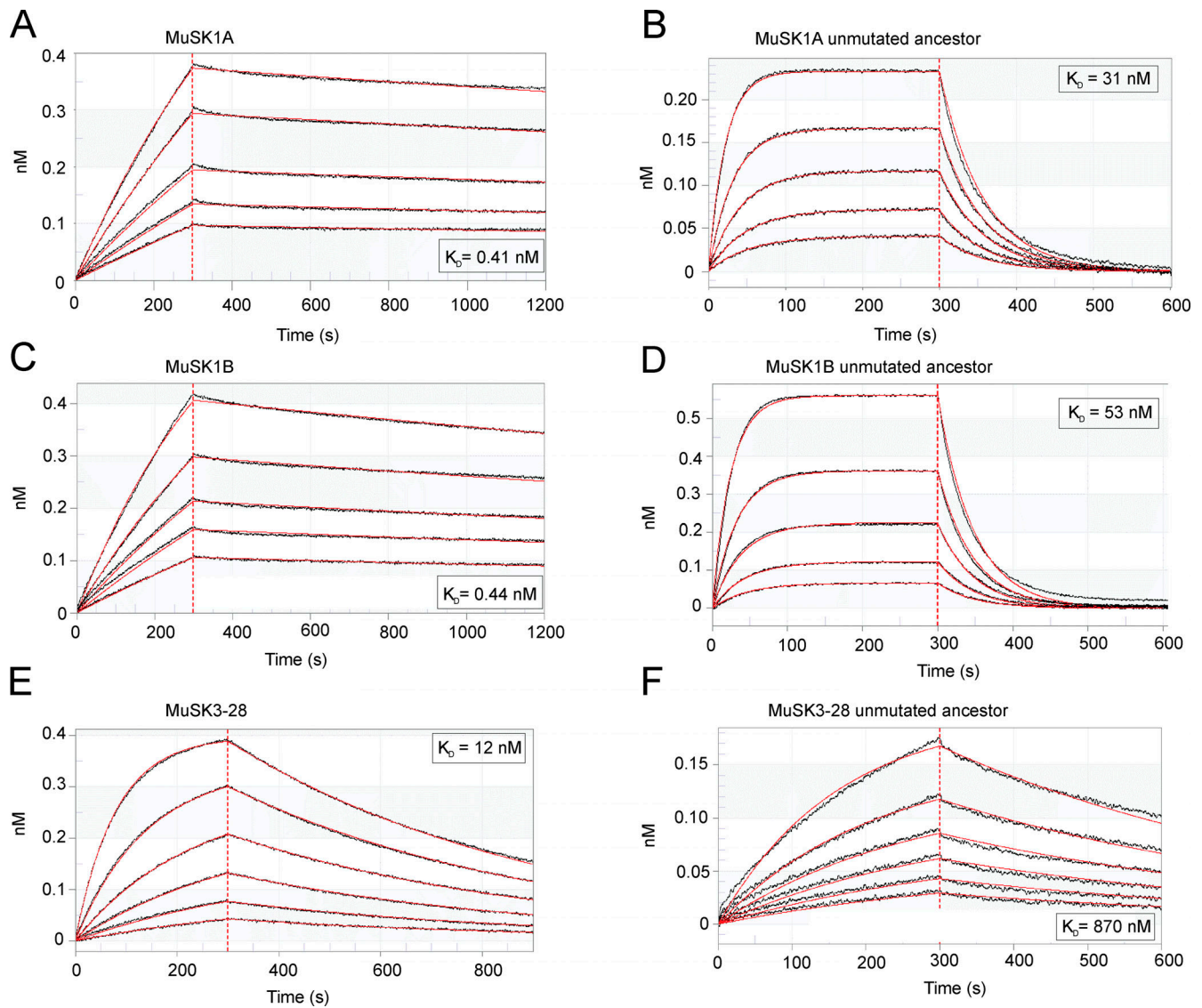


Figure S4. **The affinity of the MuSK mAb UCAs is lower than that of the mature counterpart.** Affinity of the mature and UCA Fabs to MuSK was determined by biolayer interferometry. A serial dilution series of the Fabs (900–1 nM) were used to determine the binding affinity with the captured MuSK. **(A–F)** Affinity measurements of the mature antibodies (A, C, and E) and their UCA counterparts (B, D, and F). The x axis depicts the time in seconds. The y axis depicts the wavelength shift detected by biolayer interferometry, which is proportional to material bound (nanoMolar). The K_D values are shown for each measurement.

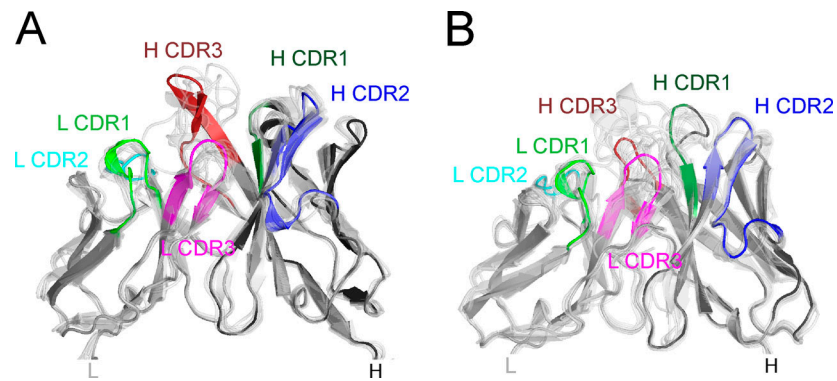


Figure S5. **MuSK1A and MuSK1B are similar to sequence-related Fabs.** MuSK1A and MuSK1B differ most substantially in the L CDR3 and H CDR3 loops compared with sequence-related Fabs from the PDB. **(A)** Superposition of VH and variable light chain (VL) domains of MuSK1A with related Fabs. PDB codes 3X3F, 3X3G, 5IES, 6DW2, 6ID4, 6MFP, 6P8N, 6MFJ, and 6PHF are aligned to the VH domain. PDB codes 4DAG, 4QHK, 4QHL, 4XNM, 4XNQ, 5ODB, 5Y2K, 6B0S, and 6EIB are aligned to the VL domain of MuSK1A. **(B)** Superposition of VH and VL domains of MuSK1B with related Fabs. PDB codes 1QLR, 3B2U, 4R4B, 5DRW, 5SX4, 5DRX, 6MLK, 6MHR, 6I19, and 6B3S are aligned to the VH domain of MuSK1B. PDB codes 4AJ0, 4AIX, 4DAG, 4QHK, 4QHL, 4XWG, 5BV7, 5ODP, 5Y2K, 6B0S, and 6EIB are aligned to the VL domain of MuSK1B.

Table S1 and Table S2 are provided online as Word files. Table S1 shows molecular characteristics of musk-binding human recombinant mAbs. Table S2 shows crystallographic data collection and refinement statistics for MuSK1A and MuSK1B.